



# Swift-heavy ion irradiation response and annealing behavior of $A_2TiO_5$ (A = Nd, Gd, and Yb)



Sulgiye Park<sup>a,\*</sup>, Cameron L. Tracy<sup>a</sup>, Fuxiang Zhang<sup>b</sup>, Raul I. Palomares<sup>c</sup>, Changyong Park<sup>d</sup>, Christina Trautmann<sup>e,f</sup>, Maik Lang<sup>c</sup>, Wendy L. Mao<sup>a,g</sup>, Rodney C. Ewing<sup>a</sup>

<sup>a</sup> Department of Geological Sciences, Stanford University, Stanford, CA 94305-2115, USA

<sup>b</sup> Materials Science and Technology Division, Oak Ridge National Laboratory, Oak Ridge, TN 37831, USA

<sup>c</sup> Department of Nuclear Engineering, University of Tennessee, Knoxville, TN 37996, USA

<sup>d</sup> High Pressure Collaborative Access Team (HPCAT), Geophysical Laboratory, Carnegie Institution of Washington, Argonne, IL 60439, USA

<sup>e</sup> GSI Helmholtzzentrum für Schwerionenforschung, 64291 Darmstadt, Germany

<sup>f</sup> Technische Universität Darmstadt, 64287 Darmstadt, Germany

<sup>g</sup> Stanford Institute for Materials & Energy Sciences, SLAC National Accelerator Laboratory, Menlo Park, CA 94025, USA

## ARTICLE INFO

### Keywords:

Ion irradiation  
High temperature  
Radiation response  
Ion tracks

## ABSTRACT

The structural responses of  $A_2BO_5$  (A = Nd, Gd, and Yb; B = Ti) compositions irradiated by high-energy Au ions (2.2 GeV) were investigated using transmission electron microscopy, synchrotron X-ray diffraction and Raman spectroscopy. The extent of irradiation-induced amorphization depends on the size of the A-site cation, with smaller lanthanides having less susceptibility to the accumulation of radiation damage. In the track-overlapping regime, complete amorphization is observed in all three compounds, despite the ability of  $Yb_2TiO_5$  to incorporate a great deal of structural disorder into its initial defect-fluorite structure ( $Fm-3m$ ). This is attributed to the high cation radius ratio (A:B = 2:1), which reduces the stability of the structure upon ion irradiation. The fully-amorphized samples were subsequently isochronally heated at temperature intervals from 100 °C to 850 °C. X-ray diffraction analysis indicated a similar damage recovery process in  $Nd_2TiO_5$  and  $Gd_2TiO_5$ , where both compositions recover their original structures ( $Pnma$ ) at 850 °C. In contrast,  $Yb_2TiO_5$  exhibited recrystallization of a metastable, non-equilibrium orthorhombic phase at ~ 550 °C, prior to a transformation to the stable defect-fluorite phase ( $Fm-3m$ ) at 625 °C. These compositional variations in radiation tolerance and thermal recovery processes are described in terms of the energetics of disordering during the damage and recrystallization processes.

## 1. Introduction

Complex oxides in the system  $A_2O_3$ - $BO_2$ , where A is a lanthanide and B is a transition metal or group 14 element, are proposed for use in a variety of technological applications due to their unique chemical and physical properties. These materials, including pyrochlore ( $A_2B_2O_6$ ) [1–6] and  $\delta$ -phase ( $A_4B_3O_{12}$ ) [7–9] compounds, have been extensively investigated as materials for nuclear waste immobilization [10–12], due to their ability to incorporate actinides and their tolerance to radiation damage when exposed to high energy particles [6,12]. Numerous studies have demonstrated that structures in this composition phase space exhibit variations in radiation stability depending on their chemical composition and bond covalency, wherein those with similar cation ionic radii (small  $r_A/r_B$ ) and primarily ionic bonding exhibit an order-disorder transformation to a defect-fluorite phase, instead of amorphization, at

high irradiation fluences [e.g., 4,5, 13–16]. Similar results were found in the system with the stoichiometry  $A_2BO_5$  (where A = lanthanide or Y, Sc; B = tetravalent or pentavalent transition metal or group 14 element), although this composition has been little investigated as compared with the pyrochlore system [17–20].

At ambient pressure,  $A_2TiO_5$  compounds exhibit three different structures, depending on composition and temperature (Fig. 1(a)). Based on the high-temperature stability diagram of Shepelev and Petrova [21], the  $A_2TiO_5$  compounds exhibit an orthorhombic structure ( $Pnma$ ) at room temperature when the A-site cation is larger than Er (A = La - Ho or Y). As illustrated in Fig. 1(b), this orthorhombic structure exhibits seven-fold coordination of A-site cations in edge-sharing mono-capped octahedra, while Ti is in five-fold coordination with oxygen in a square pyramidal configuration. When A-site cations are smaller than Er (A = Er - Lu, and Sc), a defect-fluorite structure

\* Correspondence to: 367 Panama Street, Stanford, CA 94305, USA.

E-mail address: [sulgiye@stanford.edu](mailto:sulgiye@stanford.edu) (S. Park).

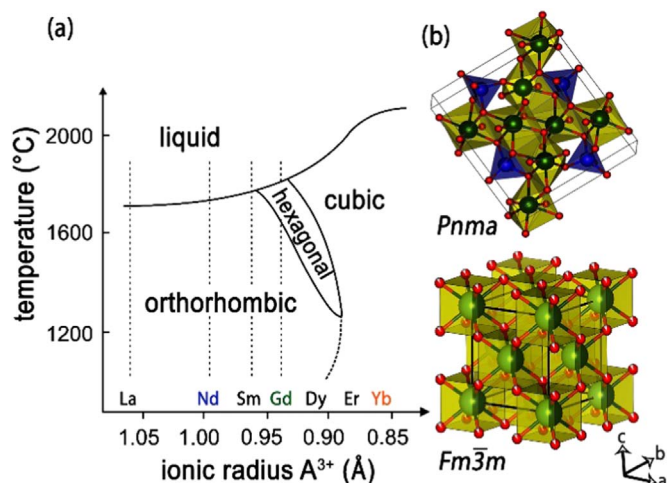


**Fig. 1.** (a) The temperature stability diagram for the series of compounds with  $A_2TiO_5$  stoichiometry, adapted from Shepelev and Petrova [21]. The compounds in this study are highlighted in red. (b) Crystal structures of orthorhombic (top) and cubic (bottom)  $A_2TiO_5$  compounds with space groups  $Pnma$  and  $Fm\bar{3}m$ , respectively. A- and B-site cations are represented by green and blue spheres, respectively. Oxygens are represented by red spheres. (For interpretation of the references to color in this figure legend, the reader is referred to the web version of this article).

( $Fm\bar{3}m$ ) is stable at room temperature, where A- and B-site cations have the same average seven-fold coordination and vacancies are randomly distributed (Fig. 1(b)). For compounds where  $A = Eu - Ho$  or  $Y$ , a hexagonal polymorph ( $P6_3/mmc$ ) with partial cation disordering is observed at temperatures above 1250 °C.

Although less investigated than  $A_2B_2O_7$  compounds,  $A_2TiO_5$  compounds have important technological applications. In addition to their possible use as nuclear waste forms,  $Nd_2TiO_5$  thin films fabricated on Si substrates find use as a part of an electrolyte-insulator-semiconductor component proposed for a high-sensitivity pH biosensing device [22].  $Gd_2TiO_5$  and  $Yb_2TiO_5$  are proposed for use in memory devices for future flash memory applications due to the high probability of charges being trapped in the deep trap energy level [23].  $Dy_2TiO_5$  is used as a neutron absorber in the control rods of Russian VVER-type reactors, due to its high melting point (~1870 °C), high neutron efficiency, insignificant swelling, and limited formation of helium bubbles [24,25].  $A_2TiO_5$  materials are also often used in thermal barrier coatings on the interior of gas turbine engines [26,27].

In some of these applications, the materials can be subjected to extreme radiation fields, which degrade their properties by generating high defect concentrations or amorphization. Many studies have investigated the radiation tolerance of  $A_2TiO_5$  materials, using low-energy ion irradiations (< 12 MeV ions) at various temperature conditions [e.g., 17–19, 28]. These studies reported that the critical temperatures for amorphization ( $T_c$ : the temperature above which structure cannot be amorphized), generally decrease for smaller  $r_A/r_B$  due to their ability to undergo order-disorder transformations with increasing ion fluences [17–19,28]. An exception to this trend was noted in  $Dy_2TiO_5$  irradiated with 12 MeV  $Au^+$  ions, for which this composition retained its initial orthorhombic structure when irradiated at temperatures above 450 °C [18].

In contrast to low-energy irradiation studies, there exist only two investigations of the effects of swift heavy ion irradiation on orthorhombic  $A_2TiO_5$  materials [20,29]. Swift heavy ions typically have energies above ~1 MeV/u and their stopping mechanism is dominated by electronic excitation and ionization processes [30,31]. This dense electronic excitation occurs over a time period of a few femtoseconds, followed by electron-phonon coupling where energy is transferred from the electronic subsystem to the atoms [30,32]. This drives the target material along the ion trajectory to a far-from-equilibrium state and produces permanently modified cylindrical zones known as the “ion

tracks”. The diameter of tracks is typically several nanometers while their length depends on the ion energy reaching several tens of micrometer or more [32,33]. In many oxides ions tracks are amorphous and the diameter of tracks is used as an indicator of the susceptibility of a specific material to radiation damage (high sensitivity results in larger track sizes). Tracy et al. [20] have demonstrated that in the electronic excitation regime, greater radiation tolerance is associated with the substitution of smaller A-site cations in  $A_2TiO_5$  materials. These results are consistent with the behavior of the same materials irradiated with low energy ions in the nuclear stopping regime [17–19]. These studies indicate that the chemical composition governs the degree of amorphization in irradiated orthorhombic  $A_2TiO_5$ , but none have addressed the influence of structure such as the behavior of cubic and orthorhombic materials with the same stoichiometry.

To clarify the role of initial structure on radiation tolerance in this system, we have compared the radiation responses of orthorhombic  $Nd_2TiO_5$  and  $Gd_2TiO_5$  with that of cubic  $Yb_2TiO_5$ . We also have investigated recrystallization during post-irradiation annealing. This study elucidates the relation between the structural response of these different compositions and structures to swift heavy ion irradiation and the subsequent thermal recovery of the radiation-induced modifications.

## 2. Experimental

Polycrystalline  $A_2TiO_5$  samples were synthesized by solid-state methods from  $A_2O_3$  and  $TiO_2$  powders. The typical grain size of the samples was several microns. The powders were then pressed into thin pellets, ground to a thickness of ~40 μm, and subsequently sintered at 800 °C for 24 h. For irradiation experiments, a small portion of the sintered pellets were carefully mounted onto a 1 cm × 1 cm aluminum plate holder using a double-sided tape. To prevent the samples from falling during the irradiation process, a thin layer of metal, resistant to melt during irradiation, was further glued on a small portion of the pellets. The pellets were irradiated at the ×0 beamline of the UNILAC linear accelerator at the GSI Helmholtz Center for Heavy Ion Research in Darmstadt, Germany. All irradiations were performed at room temperature under vacuum using 2.2 GeV Au ions and various fluences up to  $3 \times 10^{13}$  ions/cm<sup>2</sup>. To prevent bulk heating of the samples, the ion flux was maintained below  $2 \times 10^9$  ions/cm<sup>2</sup>/s<sup>1</sup>. The typical fluence uncertainty was 10–15%. SRIM-2008 code [34] was used to determine the electronic energy loss as a function of sample penetration depth (Fig. 2). The electronic energy loss (dE/dx)<sub>e</sub> for  $Yb_2TiO_5$ ,  $Gd_2TiO_5$  and  $Nd_2TiO_5$  is 44.8 keV/nm, 38.1 keV/nm and 35.01 keV/nm at the sample surface, respectively. Mass densities used for the SRIM calculations were:  $Nd_2TiO_5 = 5.73$  g/cm<sup>3</sup>;  $Gd_2TiO_5 = 6.62$  g/cm<sup>3</sup>;  $Yb_2TiO_5 = 7.96$  g/cm<sup>3</sup>. The calculations indicated projected ion ranges between 60 and 70 μm. Therefore, the 2.2 GeV Au ions passed completely through all samples. The corresponding nuclear energy loss is about three orders of magnitude smaller than the electronic energy loss and is thus assumed to be negligible.

Samples were characterized, before and after irradiation, using angle-dispersive synchrotron X-ray diffraction (XRD) and Raman spectroscopy. XRD was performed at the B2 beamline of the Cornell High Energy Synchrotron Source (CHESS), with a monochromatic beam ( $\lambda = 0.496$  Å) in transmission mode. The resulting diffraction rings were recorded with Mar charge coupled device (CCD) detectors. Confocal Raman spectroscopy was performed using a Horiba Scientific LabRAM HR Evolution spectrometer with a 20 mW HeNe laser excitation source ( $\lambda = 632.8$  nm). Samples were exposed for 30 s and 4 scans were accumulated with the collected signal averaged to obtain the final spectra.

Transmission electron microscopy (TEM) was used to determine the shapes and diameters of the ion tracks. Holey carbon-coated copper TEM grids were gently swiped over the surface of the sample pellets

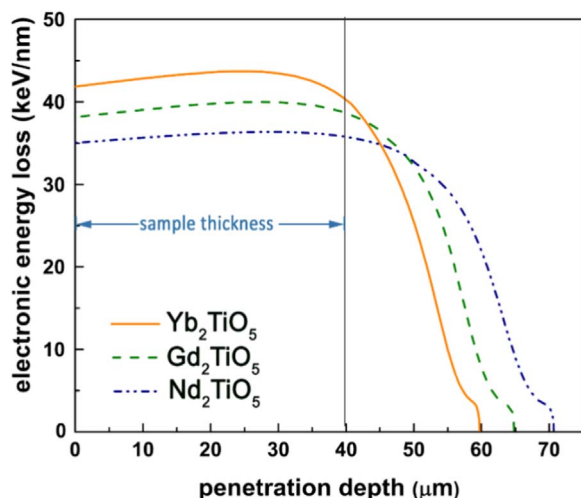


**Fig. 2.** Electronic energy loss of 2.2 GeV Au ions in  $\text{Yb}_2\text{TiO}_5$ ,  $\text{Gd}_2\text{TiO}_5$  and  $\text{Nd}_2\text{TiO}_5$  as a function of sample penetration depth. The energy loss of ions in all three materials is relatively constant across the entire  $\sim 40$   $\mu\text{m}$  thick sample (variation  $< 2$   $\mu\text{m}$ ). The ions completely penetrate through the entire sample.

after exposure to the ion beam. Samples irradiated to a fluence of  $3 \times 10^{11}$  ions/ $\text{cm}^2$  were used. At this fluence, tracks are generally well-separated, which makes it easy to analyze individual tracks. Images were collected using FEI Tecnai operating at 200 kV in a bright-field mode.

Post-irradiation isochronal annealing was performed for samples irradiated to an ion fluence of  $3 \times 10^{13}$  ions/ $\text{cm}^2$  where complete amorphization is achieved. For the annealing experiments, a hydro-thermal diamond anvil cell (HDAC) was used with the protocol described elsewhere [35]. This approach provides several advantages over the use of a conventional heating stage: (1) a stable and homogeneous heating environment [36]; (2) simultaneous annealing and characterization of multiple materials, and; (3) the ability to work with small sample sizes. To do this, small portion ( $\sim 10$   $\mu\text{m} \times 10$   $\mu\text{m}$ ) of the samples irradiated at the highest fluence ( $3 \times 10^{13}$  ions/ $\text{cm}^2$ , a fluence at which complete amorphization was achieved for all materials), were placed into a  $\sim 100$   $\mu\text{m}$  thick Re-gasket into which multiple holes of different sizes were drilled for sample identification. The samples were sealed in the gasket holder by the placement of two

diamonds on each side within a Basset-type HDAC [36], which incorporates resistive heating elements. The temperature of each diamond anvil was monitored with K-type thermocouples located near each culet. XRD measurements were collected at beamline 16-BM-D of the Advanced Photon Source (APS), Argonne National Laboratory (ANL). A monochromatic beam ( $\lambda = 0.496$   $\text{\AA}$ ) was used in transmission mode, and the diffraction rings were recorded with a mar345 image plate detector. For consistency, all three samples were simultaneously heated and measured in the same cell. The isochronal annealing measurements were collected at 50–100  $^\circ\text{C}$  intervals using a collection time of 300 s as the temperature was increased from 25  $^\circ\text{C}$  to 850  $^\circ\text{C}$ . For each temperature step, the samples were heated at the target temperature for 20 min, quenched to ambient temperature (quench time  $\sim 100$  s), and left to cool for an additional 20 min before diffraction patterns were collected.

Diffraction patterns were integrated using Dioptas [37], and Rietveld refinements of the observed XRD patterns were performed with Fullprof suite [38,39]. The background was fit with a 6th-order polynomial and the diffraction peak profile was fitted with Pseudo-Voigt functions. Atomic positions and unit cell parameters were then refined. For the thermally-induced recrystallization of  $\text{A}_2\text{TiO}_5$  samples, a broad diffuse background attributed to the back window of the HDAC configuration was measured, which manifests as a broad peak centered around  $2\theta = 7.5^\circ$  in the diffraction patterns.

In addition to Rietveld refinement, both ion-induced amorphization and thermally-induced recrystallization were further analyzed by deconvolution of the XRD peaks in order to differentiate intensity contributions from the amorphous and crystalline fractions. This procedure involved fitting the XRD patterns, where the intensities of peaks corresponding to amorphous and crystalline fractions were integrated with Pseudo-Voigt functions [5]. The ratio of the summed intensity of all crystalline peaks to the summed intensity of all amorphous and crystalline peaks was taken as the crystalline fraction,  $f_c$ .

### 3. Results and discussion

#### 3.1. Damage accumulation from swift heavy ion irradiation

A series of representative XRD patterns of  $\text{A}_2\text{TiO}_5$  materials irradiated with 2.2 GeV Au ions to fluences of up to  $3 \times 10^{13}$  ions/ $\text{cm}^2$  are shown in Fig. 3. Rietveld refinement of patterns collected from

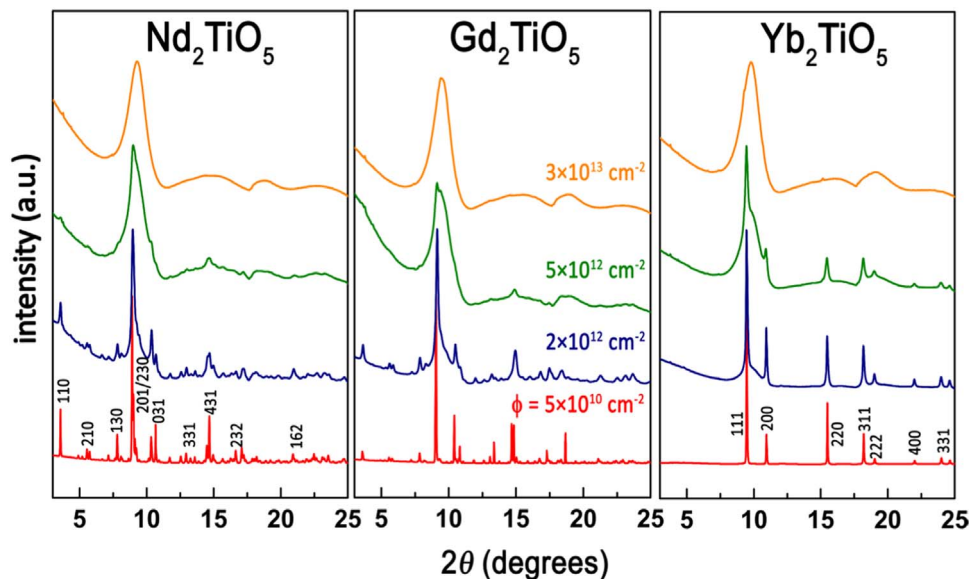


**Fig. 3.** Representative synchrotron XRD patterns ( $\lambda = 0.4967$   $\text{\AA}$ ) of 2.2 GeV Au ion irradiated  $\text{A}_2\text{TiO}_5$  compounds at various ion fluences. The XRD patterns of samples irradiated to a fluence of  $5 \times 10^{10}$  ions/ $\text{cm}^2$  do not show any changes compared to the patterns of the pristine samples.

**Table 1**

Refined unit cell parameter (from XRD patterns) and the calculated electronic energy losses at the surfaces of  $\text{Nd}_2\text{TiO}_5$ ,  $\text{Gd}_2\text{TiO}_5$ , and  $\text{Yb}_2\text{TiO}_5$ . The increased density for compounds with smaller A-site cations explains the larger electronic energy loss ( $dE/dx$ )<sub>e</sub>.

composition (space group)	a (Å)	b (Å)	c (Å)	density (g/cm <sup>3</sup> )	(dE/dx) <sub>e</sub> (keV/nm)	A-site cation ionic radius (Å)
$\text{Nd}_2\text{TiO}_5$ ( <i>Pnma</i> )	10.7	11.4	3.8	5.73	35.0	1.02
$\text{Gd}_2\text{TiO}_5$ ( <i>Pnma</i> )	10.5	11.3	3.8	6.62	38.1	0.96
$\text{Yb}_2\text{TiO}_5$ ( <i>Fm-3m</i> )	5.1	5.1	5.1	7.96	44.7	0.87

the unirradiated samples confirmed that  $\text{Nd}_2\text{TiO}_5$  and  $\text{Gd}_2\text{TiO}_5$  initially have an orthorhombic structure (*Pnma*), whereas  $\text{Yb}_2\text{TiO}_5$  has a defect fluorite structure (*Fm-3m*), consistent with the phase diagram of Shepelev and Petrova (Fig. 1a) [21]. Unit cell parameters and atomic coordinates from the refinements are listed in Table 1. The structural parameters are in good agreement with those reported previously [21,28,40].

For all three compounds, a broadening of the initial diffraction maxima is observed as a function of fluence. This peak broadening, most noticeably for the peak at  $2\theta = 8.9^\circ$ , which corresponds to overlapping (201) and (230) reflections, can be attributed to the heterogeneous microstrain around defects from atomic displacements or to the decrease in the crystallite sizes due to grain fragmentation [41]. In addition to the peak broadening, the intensity of the sharp crystalline diffraction maxima decreases monotonically as a function of ion fluence. Concurrently, the growth of wide diffuse scattering signal, characteristic of amorphous materials [42], is evident in the angular ranges  $2\theta = 8\text{--}12^\circ$ ,  $12\text{--}18^\circ$ , and  $18\text{--}21^\circ$ . Together, these changes suggest that long-range periodicity is lost. Despite the different initial structures, the peak intensities of the crystalline remnants of all materials decrease in the same systematic manner as amorphization proceeds. At the highest fluence reached ( $3 \times 10^{13}$  ions/cm<sup>2</sup>), all sharp crystalline diffraction peaks have disappeared in all three compounds.

The crystalline-to-amorphous phase transition is related to the highly localized extreme energy deposition from swift heavy ions. As energy is transferred to electrons along the ion path and electron-phonon coupling occurs, the local atomic structure is driven to a far-from-equilibrium state, causing the complete loss of long-range order and eventual relaxation to an amorphous phase. The broad bands from amorphous domains are observed in the XRD patterns and are comparable to those in  $\text{A}_2\text{TiO}_5$  [20] and  $\text{A}_2\text{Ti}_2\text{O}_7$  [5,43–45] compounds irradiated with swift heavy ions. Comparing the XRD patterns of the three compounds, the degree of amorphization at each fluence shows a pronounced dependence on composition. As illustrated by the XRD patterns for samples irradiated at a fluence of  $5 \times 10^{12}$  ions/cm<sup>2</sup> (shown in detail in Fig. 4),  $\text{Nd}_2\text{TiO}_5$  becomes nearly completely amorphous with minimal residual intensity of the crystalline peaks, while  $\text{Gd}_2\text{TiO}_5$  retains a greater crystalline fraction, seen in the splitting of sharp (crystalline) and diffuse (amorphous) peaks at  $2\theta = 8\text{--}12^\circ$ . For both of these orthorhombic compounds, however, the diffuse scattering of the amorphous phase dominates the pattern, in contrast with the cubic  $\text{Yb}_2\text{TiO}_5$ , for which the greatest degree of crystallinity is evident. While there is a broadening of the initial diffraction maxima, relatively sharp, intense peaks corresponding to the crystalline fraction are observed for  $\text{Yb}_2\text{TiO}_5$  irradiated at  $5 \times 10^{12}$  ions/cm<sup>2</sup>, at  $2\theta = 9.3^\circ$ ,  $10.7^\circ$ ,  $15.3^\circ$ , and  $17.8^\circ$ , indexed as (111), (002), (002), (113), and (222), respectively.

The compositional variation in the degree of amorphization can be more quantitatively analyzed by extracting the amorphous fraction,  $f_A$ , of the irradiation-induced amorphous phase as a function of fluence

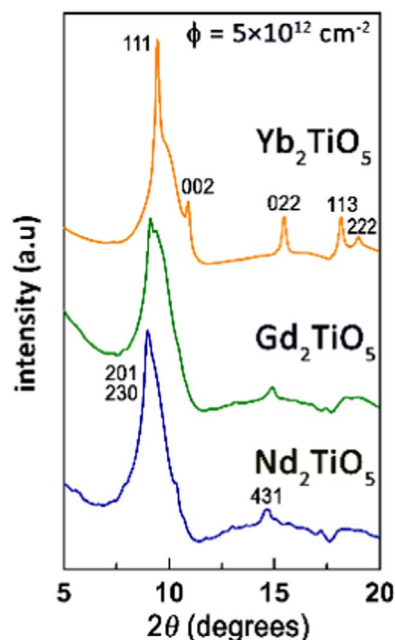


**Fig. 4.** XRD patterns ( $\lambda = 0.4967$  Å) of the three compounds irradiated at a fluence of  $5 \times 10^{12}$  ions/cm<sup>2</sup>. A greater degree of crystallinity is observed for samples with smaller A-site cations: the crystalline fraction follows the order  $\text{Yb}_2\text{TiO}_5 > \text{Gd}_2\text{TiO}_5 > \text{Nd}_2\text{TiO}_5$ .

using a deconvolution technique [5]. The procedure involved fitting the XRD patterns, where the intensities of peaks corresponding to amorphous and crystalline fractions were integrated with Pseudo-Voigt functions [5]. The integrated area of  $f_A$  at each fluence is divided by the sum of the intensities from both  $f_A$  and the crystalline fraction,  $f_C$ , (Fig. 5). Note that, due to the complex relationship between peak intensities and amorphous/crystalline phase distribution, the ratio of integrated intensities, defined as  $f_A$  and  $f_C$ , should not be treated as definitive measurements of amorphous/crystalline volume. However, similar compositions should yield similar dependences of the integrated intensities on the amorphous phase proportions induced by swift heavy ion irradiation, thus making the comparison appropriate in this case.

The analysis indicates an initial linear increase of  $f_A$  as a function of ion fluence for all materials, followed by saturation when ion tracks extensively overlap at higher fluences. Although the uncertainties are large, a trend is clear in that the track diameter increases for compounds with bigger A-site cations. However, due to the qualitative nature of the method used, the resulting track diameters should not be treated as a definitive measurement, but only as a means to compare the radiation tolerance among the materials irradiated under the controlled environment. Deviations here are the uncertainties calculated from replicating the deconvolution and fitting procedure.

The damage evolution as a function of fluence can be described by a direct-impact damage accumulation process, which indicates that each ion generates a single amorphous track as it passes through the sample [42]. The integrated intensities from the deconvolution procedure were fitted to the following direct impact equation, modeled after Gibbons [42]:

$$f_A(\Phi) = (1 - e^{-\sigma\Phi}) \quad (1)$$

where  $f_A$  represents the amorphous fraction,  $\Phi$  is the ion fluence, and  $\sigma$  is the cross-sectional area of the amorphous track produced by individual swift heavy ion. By assuming a continuous cylindrical ion track of constant track diameter, the diameter ( $d$ ) can then be estimated using:

$$\sigma = \pi \left( \frac{d}{2} \right)^2 \quad (2)$$



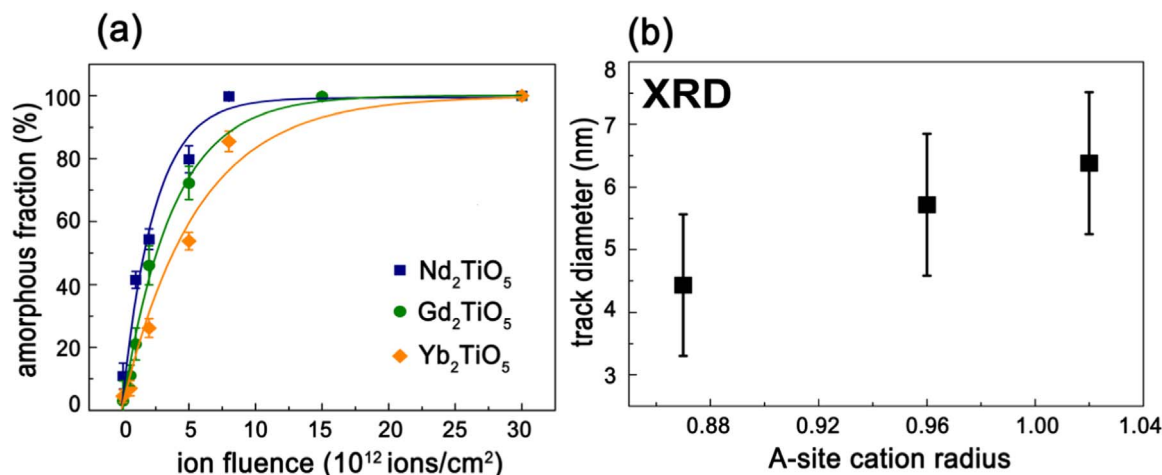


**Fig. 5.** (a) Calculated amorphous phase fractions as a function of fluence for all three compositions. The lines represent the fit of the data to a direct impact model (Eq. (1)). Error bars were derived from repeated deconvolutions of the XRD patterns. (b) The track diameters extracted from the fitting of Eq. (1) to the data. Deviations here are the uncertainties calculated from replicating the deconvolution and fitting procedure.

Ion track diameters extracted from Eq. (2) are displayed in the inset of Fig. 5. Overall, the amorphous track diameter is proportional to the size of the A-site cation. Larger track diameters are noted for those compounds with larger A-site cations (Yb<sub>2</sub>TiO<sub>5</sub>:  $d = 4.52 \pm 1.2$  nm < Gd<sub>2</sub>TiO<sub>5</sub>:  $d = 5.8 \pm 1.3$  nm < Nd<sub>2</sub>TiO<sub>5</sub>:  $d = 6.4 \pm 1.1$  nm). The A-site composition dependence of radiation tolerance can first be understood in terms of the material's propensity to form defects under irradiation. The energy of disordering,  $\Delta E_d$ , defined as the energy difference between the ordered pyrochlore and disordered defect-fluorite structure, is higher in materials with larger  $r_A/r_B$ . This is attributed to the size mismatch increases the strain necessary to accommodate site cation disordering over the A- and B-sites (cation antisite defect  $A_A + B_B \rightarrow A_B + B_A$ ) [46,47]. With the increase in the  $\Delta E_d$  via the exchange of A and B-site cations, the materials' susceptibility to amorphization increases [47]. This explains the increased susceptibility to amorphization of materials with larger  $r_A/r_B$  (Nd<sub>2</sub>TiO<sub>5</sub> and Gd<sub>2</sub>TiO<sub>5</sub>), as compared with those having smaller  $r_A/r_B$  (Yb<sub>2</sub>TiO<sub>5</sub>).

Typically, materials in the system A<sub>2</sub>O<sub>3</sub>-BO<sub>2</sub> that adopt the defect-fluorite structure prior to irradiation are highly resistant to radiation-induced amorphization [16,46–51]. However, it is interesting that Yb<sub>2</sub>TiO<sub>5</sub>, for which the initial structure is a defect-fluorite, amorphization is still observed after it had been fully irradiated. To our knowledge, this is the first study that reports swift heavy ion irradiation-induced amorphization of a defect-fluorite A<sub>2</sub>TiO<sub>5</sub>. While the overall long-range structure of the Yb<sub>2</sub>TiO<sub>5</sub> remains a defect-fluorite phase, the instability of the Yb<sub>2</sub>TiO<sub>5</sub> at higher fluences as compared with A<sub>2</sub>TiO<sub>7</sub> materials of the similar structure may be attributed to the compositional stoichiometry in that the A to B cation ratio (A:B = 2:1) is now increased as compared with the A<sub>2</sub>B<sub>2</sub>O<sub>7</sub>-type compounds (A:B = 1:1). This results in a different local distortion in the defect-fluorite structure due to random arrangements of the dissimilarly-sized cations, as well as different defect energetics due to the difficulty of fitting a large Yb in a small Ti site.]. The 'stuffing' of A-site cations causes the material to form a disordered-fluorite structure on a long-range, but the material was found to have a pyrochlore-like local ordering as investigated by neutron diffraction [52]. Whittle et al., also reported small nanoscale domains of pyrochlore form in Yb<sub>2</sub>TiO<sub>5</sub> indicated by electron diffraction patterns [40]. The inherent ordering in the short-range, then, may contribute to the increased susceptibility to radiation damage in Yb<sub>2</sub>TiO<sub>5</sub>. Under the same irradiation condition (2.2 GeV Au ions), it was found that a material of same composition, Yb<sub>2</sub>Ti<sub>2</sub>O<sub>7</sub>, which exhibits an initial pyrochlore structure (*Fd-3m*), amorphizes at a fluence of  $1.5 \times 10^{13}$  ions/cm<sup>2</sup> [16]. Conclusively, this result highlights that the stoichiometry also governs the radiation tolerance in addition to the  $r_A/r_B$ , as it affects the stability of the structure to which the material crystallizes.

Representative Raman spectra of the three compounds as a function of fluence are shown in Fig. 6. The pre-irradiation Raman spectra are consistent with those obtained in previous studies on A<sub>2</sub>TiO<sub>5</sub> compounds [20,53–55]. The low symmetry of the orthorhombic unit cell manifests itself in more than 20 Raman active modes for the isostructural Nd<sub>2</sub>TiO<sub>5</sub> and Gd<sub>2</sub>TiO<sub>5</sub> [55]. The intense Raman peak at  $\sim 780$  cm<sup>-1</sup> in both orthorhombic materials is assigned to the A<sub>g</sub> stretching mode, corresponding to the Ti-O bond in TiO<sub>5</sub> polyhedra, whereas the peaks below 350 cm<sup>-1</sup> belong to the bonds of A-site and Ti cations [55]. Another intense peak at  $\sim 360$  cm<sup>-1</sup> corresponds to a symmetric out-of-plane bending mode of O-Ti-O angles [55]. Compared to the orthorhombic Nd<sub>2</sub>TiO<sub>5</sub> and Gd<sub>2</sub>TiO<sub>5</sub>, the Raman modes in Yb<sub>2</sub>TiO<sub>5</sub> are broadened due to the random distribution of atoms on the fluorite-like sublattice in the disordered defect-fluorite phase, which makes it difficult to distinguish the peaks.

In agreement with the XRD patterns, the Raman spectra exhibit decreasing intensity of the initial sharp peaks with increasing fluence, confirming the crystalline-to-amorphous phase transformation in all materials. Surprisingly, the patterns of irradiated, fully amorphous Nd<sub>2</sub>TiO<sub>5</sub> and Gd<sub>2</sub>TiO<sub>5</sub> are comparable to that of the pristine, cubic Yb<sub>2</sub>TiO<sub>5</sub>. This suggests that despite the difference in their long-range structures, the local structure of the amorphous phase in the initially orthorhombic compounds is similar to that of the defect-fluorite phase. This is in agreement with a previous study, which reported the similarity in local structures of the amorphous and defect-fluorite phases of compounds in the A<sub>2</sub>O<sub>3</sub>-BO<sub>2</sub> system [47]. Shamblin et al., have shown that these local structures are based on orthorhombic weberite-type structural units that can be arranged into either aperiodic long-range structures or long-range structures with an average cubic symmetry [56]. While this evidence of weberite-type local ordering has been reported for disordered and amorphous A<sub>2</sub>B<sub>2</sub>O<sub>7</sub>-type pyrochlore compounds [47,56], the present study further substantiates the similar local structures in A<sub>2</sub>TiO<sub>5</sub> compounds.

Considering the unusual observation of irradiation-induced amorphization of a defect-fluorite compound, the morphology of ion tracks induced by 2.2 GeV Au ions ( $3 \times 10^{11}$  ions/cm<sup>2</sup>) in Yb<sub>2</sub>TiO<sub>5</sub> was investigated using transmission electron microscopy (Fig. 7). In the bright-field image (Fig. 7a), the tracks show a darker contrast embedded in the lighter surrounding matrix. Ion track diameters were estimated by determining the position of the parallel boundaries between the modified contrast and the pristine matrix. A total of  $\sim 30$  tracks were measured in several images collected using multiple grains of the same sample, in order to eliminate orientation effects. The mean diameter of the tracks is  $d = 7.1 \pm 0.8$  nm. The track diameters determined by TEM are larger than those determined

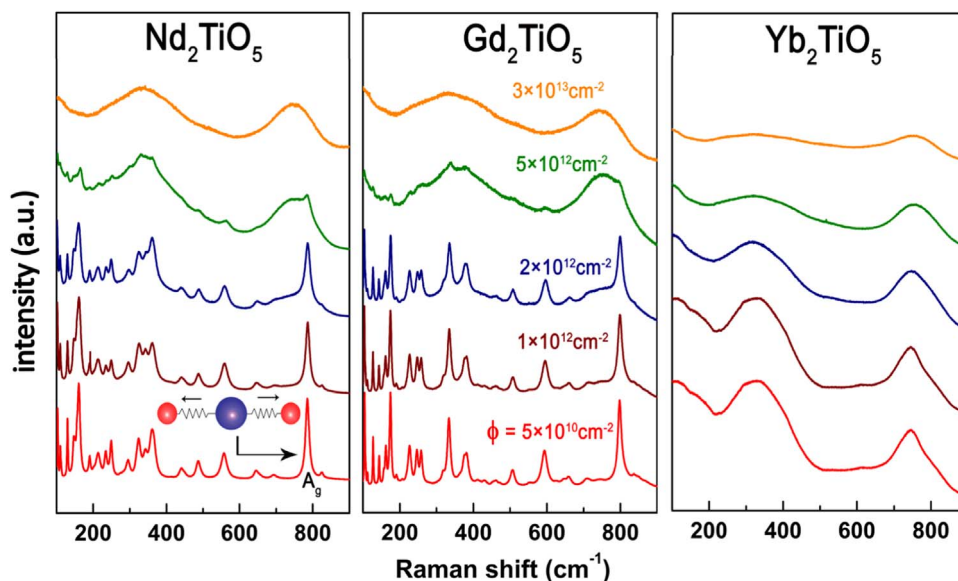


**Fig. 6.** Representative Raman spectra of 2.2 GeV Au ion irradiated  $A_2TiO_5$  compounds at various fluences. As a function of increasing fluence, the spectra of all three compounds exhibit gradual loss of the initial vibrational modes, which are then accompanied by the growth of broad bands, indicating a crystalline-to-amorphous phase transformation.

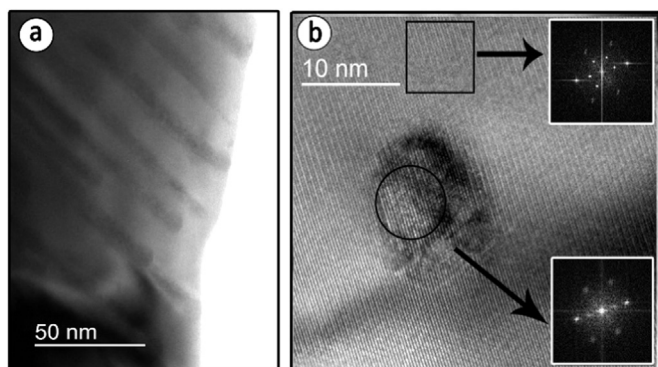


**Fig. 7.** (a) Bright-field TEM image of ion tracks of  $Yb_2TiO_5$  induced by 2.2 GeV  $^{196}Au$  ions at a fluence of  $3 \times 10^{11}$  ions/cm<sup>2</sup>. The well separated and parallel oriented ion tracks appear with a darker contrast than the surrounding undamaged matrix. (b) HRTEM image of the cross section of a single track revealing the heterogeneous damage morphology. The insets represent the FFT analysis of the in-track and surrounding matrix phases.

using XRD patterns (XRD:  $d = 4.5 \pm 1.2$  nm). This discrepancy is attributed to the fact that the contrast in the bright-field TEM images includes the disordered phase surrounding the core, whereas XRD only measures the signal arising from the increasing amorphous contribution to the background [4]. To better observe the damage structure within the ion tracks, the cross-sections of the tracks were imaged by high-resolution TEM (HRTEM) revealing ion tracks in  $Yb_2TiO_5$  (Fig. 7b). Fast Fourier transform (FFT) analyses (insets in Fig. 7b) indicates a disordered crystalline phase. Previous experimental and computational studies on  $Gd_2TiO_5$  ion tracks showed a disordered shell surrounding an amorphous track core [29,57]. Our TEM image does not show a definitive shell surrounding the amorphous core, which could be attributed to the long range defect-fluorite phase of the  $Yb_2TiO_5$ . Instead, its heterogeneous track morphology is more comparable to that observed in  $Nd_2Zr_2O_7$  pyrochlore irradiated with 120 MeV U ions, where the individual ion tracks were shown to consist of both amorphous and defect-fluorite phases at any fluence without a core-shell structure [58].

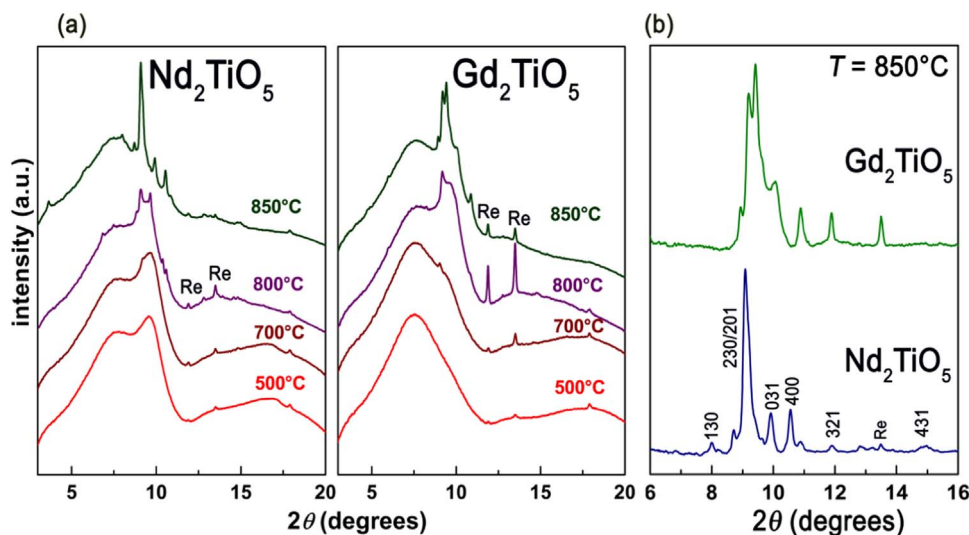


**Fig. 8.** (a) Representative XRD patterns of  $Nd_2TiO_5$  and  $Gd_2TiO_5$  as a function of temperature. The pronounced crystalline peaks at  $2\theta = 12^\circ$  and  $14^\circ$  are from the rehenium sample holder inside the HDAC. (b) XRD patterns of the two compositions at 850 °C after background subtraction.

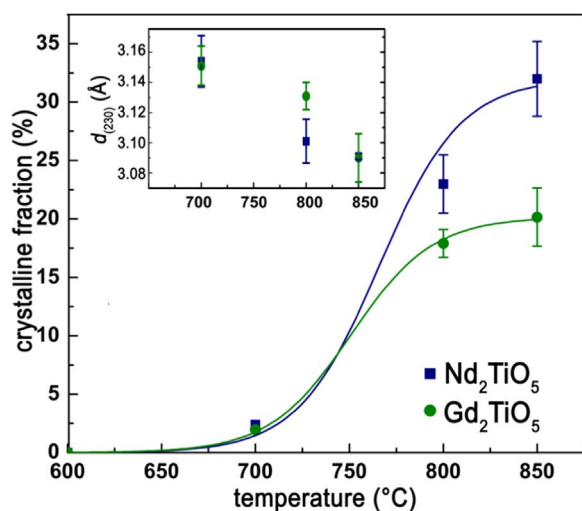


**Fig. 9.** Calculated crystalline fraction as a function of temperature for  $\text{Nd}_2\text{TiO}_5$  and  $\text{Gd}_2\text{TiO}_5$ . The solid lines are a guide for the eye. (Inset) The  $d$ -spacing associated with the (230) peak position with increasing temperature. Error bars in this figure indicate the  $d$ -spacing range corresponding to FWHM value of each (230) peak.

### 3.2. Damage recovery with isochronal annealing

Annealing was performed on completely amorphized samples in order to induce recrystallization. XRD characterization of the isochronal recovery behavior as a function of temperature is illustrated in Figs. 8 and 9. With increasing annealing temperature,  $\text{Nd}_2\text{TiO}_5$  and  $\text{Gd}_2\text{TiO}_5$  undergo an isomorphic phase recovery, where their initial orthorhombic structures are recovered (Fig. 8a). In the low temperature regime the broad, diffuse scattering bands from the back window of the sample chamber dominate the XRD patterns of both compositions, but the trend that  $\text{Nd}_2\text{TiO}_5$  exhibits more pronounced crystalline peaks than  $\text{Gd}_2\text{TiO}_5$  at each temperature is evident. This is more obvious when the diffuse scattering from the HDAC window contribution is subtracted (at higher temperatures when scattering intensity from the samples are higher than that from the chamber window) for the purpose of refinement. Fig. 8b illustrates this effect at an annealing temperature of 850 °C, where  $\text{Nd}_2\text{TiO}_5$  clearly exhibits more pronounced crystalline peaks at  $2\theta = 7.9^\circ, 9.1^\circ, 9.8^\circ, 10.5^\circ$  and  $15.0^\circ$  compared with those from  $\text{Gd}_2\text{TiO}_5$ . For further analysis, XRD patterns were, again, deconvoluted into amorphous and crystalline contributions – the same procedure used to analyze the radiation-induced amorphization. Due to the limited recrystallization of the two compounds at lower temperatures, only the patterns above 600 °C were analyzed after the background had been subtracted. Despite the small number of data points, there is a clear difference between the two compounds, wherein  $\text{Nd}_2\text{TiO}_5$  displays a greater  $f_c$  at a given temperature as compared with  $\text{Gd}_2\text{TiO}_5$  (Fig. 9).

The lower annealing temperature of  $\text{Nd}_2\text{TiO}_5$  as compared with  $\text{Gd}_2\text{TiO}_5$  suggests that the energy barrier for recrystallization is lower in  $\text{Nd}_2\text{TiO}_5$  over this temperature range. This is not consistent with the compositional trend generally observed in irradiation-induced amorphization. As described above,  $\text{Nd}_2\text{TiO}_5$  is more susceptible to radiation damage due to its higher  $r_A/r_B$ . In terms of annealing,  $\text{Nd}_2\text{TiO}_5$ , which is more prone to undergo the crystalline-to-amorphous transition, also has a lower energy barrier for the reverse transformation, as compared with  $\text{Gd}_2\text{TiO}_5$ . While numerous studies have reported that materials with higher  $r_A/r_B$  and increased energy for disordering tend to amorphize more easily, this study shows that materials with increased susceptibility to radiation damage may also be more likely to recrystallize during post-irradiation annealing.

Unlike the orthorhombic  $\text{A}_2\text{TiO}_5$  materials,  $\text{Yb}_2\text{TiO}_5$  exhibits a multi-phase (polymorphic) recrystallization with increasing temperature (Fig. 10).  $\text{Yb}_2\text{TiO}_5$  initially recrystallizes at ~ 500 °C (not shown in

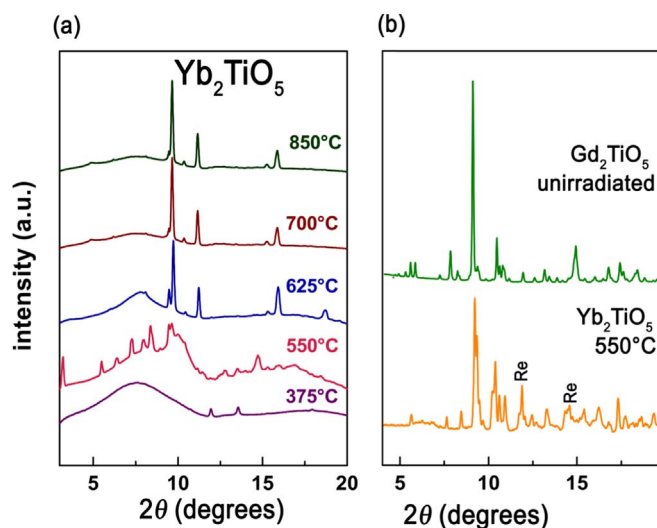


**Fig. 10.** (a) Representative XRD patterns of  $\text{Yb}_2\text{TiO}_5$  as a function of temperature. The composition exhibits a multi-phase structural transformation where the amorphous phase first forms an orthorhombic phase similar to that of  $\text{Gd}_2\text{TiO}_5$  and  $\text{Nd}_2\text{TiO}_5$ , followed by recovery of the initial cubic phase. (b) Background subtracted XRD pattern of  $\text{Yb}_2\text{TiO}_5$  annealed at 550 °C, compared with that of unirradiated  $\text{Gd}_2\text{TiO}_5$ .

the figure) in an orthorhombic structure, before undergoing a crystalline-to-crystalline transformation to the stable cubic defect-fluorite structure through a reconstructive transformation at temperatures above 625 °C. Refinement showed the initially recrystallized orthorhombic phase to be comparable to the orthorhombic phase of  $\text{Nd}_2\text{TiO}_5$  and  $\text{Gd}_2\text{TiO}_5$ . By 550 °C, the XRD profile shows peaks belonging to both the orthorhombic and cubic phases. Complete recovery of the defect-fluorite structure occurs at a temperature above 625 °C, at which point diffraction peaks belonging to the orthorhombic phase disappear. This multi-phase recrystallization process depends on the energy difference between the amorphous phase and the possible crystalline phases, along with the kinetics of the atomic rearrangements necessary to reach the different crystalline structures. This phase transition pathway can be attributed to the fact that the transition from the amorphous to the orthorhombic phase requires a lower activation energy than would the immediate formation of the stable defect-fluorite phase, due to fewer topological constraints from the smaller degree of atomic connectivity of the orthorhombic structure. Only after the energy barrier to rearrangement into a high-symmetry defect-fluorite structure is overcome, at a higher temperature, is the equilibrium cubic phase formed. The metastable phase formation also follows Ostwald's rule, which states that recrystallization tends to first yield the least stable accessible phase of a system prior to eventual formation of more stable phases [59]. The polymorphic phase recovery of  $\text{Yb}_2\text{TiO}_5$  is very similar to that noted in Cm-doped  $\text{CaZrTi}_2\text{O}_7$  after it had been damaged by recoil-nuclei and alpha particles [60]. With isochronal heating,  $\text{CaZrTi}_2\text{O}_7$  initially recovered to a metastable rhombohedral phase, followed by a final stable monoclinic structure.

## 4. Summary

The radiation tolerance (*i.e.*, the ability to remain crystalline under energetic ion irradiation) and annealing behavior of  $\text{A}_2\text{TiO}_5$  ( $\text{A} = \text{Nd}, \text{Gd}, \text{and Yb}$ ) compounds have been investigated. The structural evolution of these materials induced by dense electronic excitation depends on the composition, particularly the cation radius ratio, as well as the interaction strength between the cations and neighboring anions. With 2.2 GeV Au ion irradiation, all compounds undergo crystalline-to-amorphous phase transitions. The extent of this transformation, as a function of ion fluence, is proportional to the ionic radius of the A-site cation. The susceptibility to amorphization was greatest in  $\text{Nd}_2\text{TiO}_5$ ,



followed by  $\text{Gd}_2\text{TiO}_5$  and  $\text{Yb}_2\text{TiO}_5$ . Raman spectra demonstrate that in terms of local structure the amorphous phases of these compounds are similar to the defect-fluorite phase. Our study is the first observation of amorphization of a compound with an initial defect-fluorite structure,  $\text{Yb}_2\text{TiO}_5$ . Radiation susceptibility in Ti-rich ternary oxides is an interplay between the A-site vacancies, B-site (Ti) interstitials, and mobile oxygen vacancies. As is the case of structurally/compositionally related  $\text{A}_2\text{Ti}_2\text{O}_7$  compounds, an excess of A-site vacancies and B-site (Ti) interstitials accumulate with increased dose, which leads to amorphization in  $\text{A}_2\text{TiO}_5$  materials. The results here lend support to the previous findings that with increased A-site cation size, the anion diffusion is reduced, and the cation defect accumulation enhances migration barriers for anions, which leads to less effective anion defect annihilation [61–63].

With isochronal annealing, all three swift heavy ion irradiation-amorphized  $\text{A}_2\text{TiO}_5$  compounds exhibit recrystallization to their original structures. Materials with increased susceptibility to radiation damage are more prone to recrystallization during post-irradiation annealing.  $\text{Nd}_2\text{TiO}_5$  and  $\text{Gd}_2\text{TiO}_5$  recrystallize back to their initial orthorhombic structure, although the relatively low symmetry kinetically constrains recrystallization at temperatures below 700 °C. In contrast,  $\text{Yb}_2\text{TiO}_5$  exhibits a multi-phase structural transition, where a non-equilibrium orthorhombic phase, isostructural to those of  $\text{Nd}_2\text{TiO}_5$  and  $\text{Gd}_2\text{TiO}_5$ , forms at lower temperatures (~ 550 °C), before a transformation to the more stable cubic defect-fluorite phase at higher temperatures (625° and above).

## Acknowledgements

This work was supported by the Energy Frontier Research Center *Materials Science of Actinides* funded by the U.S. Department of Energy (DOE), Office of Science, Office of Basic Energy Sciences (Grant no. DE-SC0001089). Part of this work was performed at HPCAT (Sector 16), Advanced Photon Source (APS), Argonne National Laboratory. HPCAT operations are supported by DOE-NSA under Award no. DE-NA0001974 and DOE-BES under Award no. DE-FG02-99ER45775, with partial instrumentation funding by NSF. The Advanced Photon Source is a U.S. Department of Energy (DOE) Office of Science User Facility operated for the DOE Office of Science by Argonne National Laboratory under Contract No. DE-AC02-06CH1135. Use of the Advanced Photon Source was supported by the Carnegie/Department of Energy Alliance Center (CDAC, DE-FC03-03NA00144).

## References

- J. Lian, L.M. Wang, S.X. Wang, J. Chen, L.A. Boatner, R.C. Ewing, Nanoscale manipulation of pyrochlore: new nanocomposite ionic conductors, *Phys. Rev. Lett.* 87 (2001) 3–6. <http://dx.doi.org/10.1103/PhysRevLett.87.145901>.
- J. Lian, L. Wang, J. Chen, K. Sun, R.C. Ewing, J.M. Farmer, L.A. Boatner, The order-disorder transition in ion-irradiated pyrochlore, *Acta Mater.* 51 (2003) 1493–1502. [http://dx.doi.org/10.1016/S1359-6454\(02\)00544-X](http://dx.doi.org/10.1016/S1359-6454(02)00544-X).
- J. Lian, J. Chen, L. Wang, R. Ewing, J. Farmer, L. Boatner, K. Helean, Radiation-induced amorphization of rare-earth titanate pyrochlores, *Phys. Rev. B* 68 (2003) 134107. <http://dx.doi.org/10.1103/PhysRevB.68.134107>.
- M. Lang, J. Lian, J. Zhang, F. Zhang, W.J. Weber, C. Trautmann, R.C. Ewing, Single-ion tracks in  $\text{Gd}_2\text{Zr}_2\text{-xTi}_x\text{O}_7$  pyrochlores irradiated with swift heavy ions, *Phys. Rev. B – Condens. Matter Mater. Phys.* 79 (2009) 1–9. <http://dx.doi.org/10.1103/PhysRevB.79.224105>.
- M. Lang, F.X. Zhang, R.C. Ewing, J. Lian, C. Trautmann, Z. Wang, Structural modifications of  $\text{Gd}_2\text{Zr}_2\text{-xTi}_x\text{O}_7$  pyrochlore induced by swift heavy ions: disordering and amorphization, *J. Mater. Res.* 24 (2009) 1322–1334. <http://dx.doi.org/10.1557/jmr.2009.0151>.
- S.X. Wang, B.D. Begg, L.M. Wang, R.C. Ewing, W.J. Weber, K.V.G. Kutty, Radiation stability of gadolinium zirconate: a waste form for plutonium disposition, *J. Mater. Res.* 14 (1999) 4470–4473. <http://dx.doi.org/10.1557/JMR.1999.0606>.
- M. Tang, P. Kluth, J. Zhang, M.K. Patel, B.P. Uberuaga, C.J.O. Reichhardt, K.E. Sickafus, Swift heavy ion irradiation-induced microstructure modification of two delta-phase oxides:  $\text{Sc}_4\text{Zr}_3\text{O}_{12}$  and  $\text{Lu}_4\text{Zr}_3\text{O}_{12}$ , *Nucl. Instrum. Methods Phys. Res. Sect. B Beam Interact. Mater. Atoms* 268 (2010) 3243–3247. <http://dx.doi.org/10.1016/j.nimb.2010.05.099>.
- M. Tang, T.A. Wynn, M.K. Patel, J. Won, I. Monnet, J.C. Pivin, N.A. Mara, K.E. Sickafus, Structure and mechanical properties of swift heavy ion irradiated tungsten-bearing delta-phase oxides  $\text{Y}_6\text{W}_{10}\text{O}_{12}$  and  $\text{Y}_6\text{W}_{10}\text{O}_{12}$ , *J. Nucl. Mater.* 425 (2012) 193–196. <http://dx.doi.org/10.1016/j.jnucmat.2011.11.029>.
- M. Ishimaru, Y. Hirotsu, M. Tang, J.A. Valdez, K.E. Sickafus, Ion-beam-induced phase transformations in  $\delta\text{-Sc}_4\text{Zr}_3\text{O}_{12}$ , *J. Appl. Phys.* 102 (2007) 063532. <http://dx.doi.org/10.1063/1.2783892>.
- R.C. Ewing, W.J. Weber, J. Lian, Nuclear waste disposal-pyrochlore ( $\text{A}_2\text{B}_2\text{O}_7$ ): nuclear waste form for the immobilization of plutonium and “minor” actinides, *J. Appl. Phys.* 95 (2004) 5949–5971. <http://dx.doi.org/10.1063/1.1707213>.
- R.C. Ewing, W.J. Weber, F.W. Clinard, Radiation effects in nuclear waste forms for high-level radioactive waste, *Prog. Nucl. Energy* 29 (1995) 63–127. [http://dx.doi.org/10.1016/0149-1970\(94\)00016-Y](http://dx.doi.org/10.1016/0149-1970(94)00016-Y).
- W.J. Weber, R.C. Ewing, C.R.A. Catlow, T.D. de la Rubia, L.W. Hobbs, C. Kinoshita, H. Matzke, A.T. Motta, M. Nastasi, E.K.H. Salje, E.R. Vance, S.J. Zinkle, Radiation effects in crystalline ceramics for the immobilization of high-level nuclear waste and plutonium, *J. Mater. Res.* 13 (1998) 1434–1484. <http://dx.doi.org/10.1557/JMR.1998.0205>.
- K. Trachenko, Understanding resistance to amorphization by radiation damage, *J. Phys. Condens. Matter* 16 (2004) R1491–R1515. <http://dx.doi.org/10.1088/0953-8984/16/49/R03>.
- K. Trachenko, M. Pruneda, E. Artacho, M.T. Dove, Radiation damage effects in the perovskite  $\text{CaTiO}_3$  and resistance of materials to amorphization, *Phys. Rev. B – Condens. Matter Mater. Phys.* 70 (2004) 1–6. <http://dx.doi.org/10.1103/PhysRevB.70.134112>.
- H.M. Naguib, R. Kelly, Criteria for bombardment-induced structural changes in non-metallic solids, *Radiat. Eff.* 25 (1975) 1–12. <http://dx.doi.org/10.1080/00337577508242047>.
- J. Shamblin, C.L. Tracy, R.C. Ewing, F. Zhang, W. Li, C. Trautmann, M. Lang, Structural Response of Titanate Pyrochlores to Swift Heavy Ion Irradiation, *Acta Mater.* 117 (2016) 207–215. <http://dx.doi.org/10.1016/j.actamat.2016.07.017>.
- K.R. Whittle, G.R. Lumpkin, M.G. Blackford, R.D. Aughterson, K.L. Smith, N.J. Zaluzec, Ion-beam irradiation of lanthanum compounds in the systems  $\text{La}_2\text{O}_3\text{-Al}_2\text{O}_3$  and  $\text{La}_2\text{O}_3\text{-TiO}_2$ , *J. Solid State Chem.* 183 (2010) 2416–2420. <http://dx.doi.org/10.1016/j.jssc.2010.07.033>.
- R.D. Aughterson, G.R. Lumpkin, M. Ionescu, M. De Los Reyes, B. Gault, K.R. Whittle, K.L. Smith, J.M. Cairney, Ion-irradiation resistance of the orthorhombic  $\text{Ln}_2\text{TiO}_5$  ( $\text{Ln} = \text{La, Pr, Nd, Sm, Eu, Gd, Tb and Dy}$ ) series, *J. Nucl. Mater.* 467 (2015) 683–691. <http://dx.doi.org/10.1016/j.jnucmat.2015.10.028>.
- J. Zhang, F. Zhang, M. Lang, F. Lu, J. Lian, R.C. Ewing, Ion-irradiation-induced structural transitions in orthorhombic  $\text{Ln}_2\text{TiO}_5$ , *Acta Mater.* 61 (2013) 4191–4199. <http://dx.doi.org/10.1016/j.actamat.2013.03.045>.
- C.L. Tracy, M. Lang, J. Zhang, F. Zhang, Z. Wang, R.C. Ewing, Structural response of  $\text{A}_2\text{TiO}_5$  ( $\text{A} = \text{La, Nd, Sm, Gd}$ ) to swift heavy ion irradiation, *Acta Mater.* 60 (2012) 4477–4486. <http://dx.doi.org/10.1016/j.actamat.2012.05.005>.
- Y.F. Shepelev, M.A. Petrova, Crystal structures of  $\text{Ln}_2\text{TiO}_5$  ( $\text{Ln} = \text{Gd, Dy}$ ) polymorphs, *Inorg. Mater.* 44 (2008) 1354–1361. <http://dx.doi.org/10.1134/S0020168508120170>.
- T.M. Pan, J.C. Lin, M.H. Wu, C.S. Lai, Structural properties and sensing performance of high-k  $\text{Nd}_2\text{TiO}_5$  thin layer-based electrolyte-insulator-semiconductor for pH detection and urea biosensing, *Biosens. Bioelectron.* 24 (2009) 2864–2870. <http://dx.doi.org/10.1016/j.bios.2009.02.018>.
- Y. Jiang, J.R. Smith, G. Robert Odette, Prediction of structural, electronic and elastic properties of  $\text{Y}_2\text{Ti}_2\text{O}_7$  and  $\text{Y}_2\text{TiO}_5$ , *Acta Mater.* 58 (2010) 1536–1543. <http://dx.doi.org/10.1016/j.actamat.2009.10.061>.
- V.D. Risovany, E.E. Varlashova, D.N. Suslov, Dysprosium titanate as an absorber material for control rods, *J. Nucl. Mater.* 281 (2000) 84–89. [http://dx.doi.org/10.1016/S0022-3115\(00\)00129-X](http://dx.doi.org/10.1016/S0022-3115(00)00129-X).
- A. Sinha, B.P. Sharma, Development of dysprosium titanate based ceramics, *J. Am. Ceram. Soc.* 88 (2005) 1064–1066. <http://dx.doi.org/10.1111/j.1551-2916.2005.00211.x>.
- P.K. Schelling II, S.R. Phillpot, R.W. Grimes, Optimum pyrochlore compositions for low thermal conductivity, *Philos. Mag. Lett.* 84 (2004) 127–137. <http://dx.doi.org/10.1080/09500830310001646699>.
- J. Wu, X. Wei, N.P. Padture, P.G. Klemens, M. Gell, E. García, P. Miranzo, M.I. Osendi, Low-thermal-conductivity rare-earth zirconates for potential thermal-barrier coating applications, *J. Am. Ceram. Soc.* 85 (2002) 3031–3035. <http://dx.doi.org/10.1111/j.1151-2916.2002.tb00574.x>.
- R.D. Aughterson, G.R. Lumpkin, G.J. Thorogood, Z. Zhang, B. Gault, J.M. Cairney, Crystal chemistry of the orthorhombic  $\text{Ln}_2\text{TiO}_5$  compounds with  $\text{Ln} = \text{La, Pr, Nd, Sm, Gd, Tb and Dy}$ , *J. Solid State Chem.* 227 (2015) 60–67. <http://dx.doi.org/10.1016/j.jssc.2015.03.003>.
- J. Zhang, M. Lang, R.C. Ewing, R. Devanathan, W.J. Weber, M. Toulemonde, Nanoscale phase transitions under extreme conditions within an ion track, *J. Mater. Res.* 25 (2010) 1344–1351. <http://dx.doi.org/10.1557/JMR.2010.0180>.
- A.V. Lankin, I.V. Morozov, G.E. Norman, S.A. Pikuz, I. Yu Skobelev, Solid-Density Plasma Nanochannel Generated by a Fast Single Ion in Condensed Matter, *Phys. Rev. E* 79 (2009) 0364107. <http://dx.doi.org/10.1103/PhysRevE.79.036407>.
- F.F. Komarov, N. Itoh, D.M. Duffy, S. Khakshouri, A.M. Stoneham, Defect and track formation in solids irradiated by superhigh-energy ions Making tracks: electronic excitation roles in forming swift heavy ion tracks making tracks: electronic excitation roles in forming swift heavy ion tracks, *J. Phys. Condens. Matter* 21 (2009) 474205–474214. <http://dx.doi.org/10.1088/0953-8984/21/47/474205>.
- M. Lang, R. Devanathan, M. Toulemonde, C. Trautmann, Advances in understanding of swift heavy-ion tracks in complex ceramics, *Curr. Opin. Solid State Mater. Sci.* 19 (2015) 39–48. <http://dx.doi.org/10.1016/j.cossms.2014.10.002>.



- [33] M. Toulemonde, W. Assmann, C. Dufour, A. Meftah, C. Trautmann, Nanometric transformation of the matter by short and intense electronic excitation: experimental data versus inelastic thermal spike model, *Nucl. Instrum. Methods Phys. Res. Sect. B Beam Interact. Mater. Atoms* 277 (2012) 28–39. <http://dx.doi.org/10.1016/j.nimb.2011.12.045>.
- [34] J.F. Ziegler, M.D. Ziegler, J.P. Biersack, SRIM – the stopping and range of ions in matter (2010), *Nucl. Instrum. Methods Phys. Res. Sect. B Beam Interact. Mater. Atoms* 268 (2010) 1818–1823. <http://dx.doi.org/10.1016/j.nimb.2010.02.091>.
- [35] R.I. Palomares, C.L. Tracy, F. Zhang, C. Park, D. Popov, C. Trautmann, R.C. Ewing, M. Lang, In situ defect annealing of swift heavy ion irradiated CeO<sub>2</sub> and ThO<sub>2</sub> using synchrotron X-ray diffraction and a hydrothermal diamond anvil cell, *J. Appl. Cryst.* 48 (2015) 711–717. <http://dx.doi.org/10.1107/S160057671500477X>.
- [36] W.A. Bassett, High pressure-temperature aqueous systems in the hydrothermal diamond anvil cell (HDAC), *Eur. J. Mineral.* 15 (2003) 773–780. <http://dx.doi.org/10.1127/0935-1221/2003/0015-0773>.
- [37] C. Prescher, V.B. Prakapenka, DIOPTAS: a program for reduction of two-dimensional X-ray diffraction data and data exploration, *High Press. Res.* 7959 (2015) 1–8. <http://dx.doi.org/10.1080/08957959.2015.1059835>.
- [38] J. Rodriguez-Carvajal, Fullprof suite, LLB Sacleys LCSIM Rennes. Fr., 2003.
- [39] T. Roisnel, J. Rodriguez-Carvajal, WinPLOTR: a windows tool for powder diffraction pattern analysis, *Mater. Sci. Forum* 378–381 (2001) 118–123. <http://dx.doi.org/10.4028/www.scientific.net/MSF.378-381>.
- [40] K.R. Whittle, M.G. Blackford, R.D. Aughterson, G.R. Lumpkin, N.J. Zaluzec, Ion irradiation of novel yttrium/ytterbium-based pyrochlores: the effect of disorder, *Acta Mater.* 59 (2011) 7530–7537. <http://dx.doi.org/10.1016/j.actamat.2011.09.021>.
- [41] L. Zhang, W. Jiang, A. Dissanayake, X. Qiu-Rong, Z. Jian, Y. Dong-Min, G. Qi-Xun, L. Ning, Grain growth of nanocrystalline 3C-SiC under Au ion irradiation at elevated temperatures Krypton ion irradiation-induced amorphization and nanocrystal formation in pyrochlore Lu<sub>2</sub>Ti<sub>2</sub>O<sub>7</sub> at room temperature, *Chin. Phys. B* 24 (2015) 126103. <http://dx.doi.org/10.1088/1674-1056/24/12/126103>.
- [42] J.F. Gibbons, Ion implantation in semiconductors. Part II: damage production and annealing, *Proc. IEEE* 60 (1972) 1062–1096. <http://dx.doi.org/10.1109/PROC.1972.8854>.
- [43] G. Sattonnay, S. Moll, L. Thomé, C. Legros, A. Calvo, M. Herbst-Ghysel, C. Decorse, I. Monnet, Effect of composition on the behavior of pyrochlores irradiated with swift heavy ions, *Nucl. Instrum. Methods Phys. Res. Sect. B Beam Interact. Mater. Atoms* (2012) 261–265. <http://dx.doi.org/10.1016/j.nimb.2011.01.079>.
- [44] G. Sattonnay, S. Moll, L. Thomé, C. Decorse, C. Legros, P. Simon, J. Jagielski, I. Jozwik, I. Monnet, Phase transformations induced by high electronic excitation in ion-irradiated Gd<sub>2</sub>(Zr<sub>x</sub>Ti<sub>1-x</sub>)<sub>2</sub>O<sub>7</sub> pyrochlores, *J. Appl. Phys.* 108 (2010) 103512. <http://dx.doi.org/10.1063/1.3503452>.
- [45] M.K. Patel, V. Vijayakumar, S. Kailas, D.K. Avasthi, J.C. Pivin, A.K. Tyagi, Structural modifications in pyrochlores caused by ions in the electronic stopping regime, *J. Nucl. Mater.* 380 (2008) 93–98. <http://dx.doi.org/10.1016/j.jnucmat.2008.07.007>.
- [46] K.E. Sickafus, R.W. Grimes, J.A. Valdez, A. Cleave, M. Tang, M. Ishimaru, S.M. Corish, C.R. Stanek, B.P. Uberuaga, Radiation-induced amorphization resistance and radiation tolerance in structurally related oxides, *Nat. Mater.* 6 (2007) 217–223. <http://dx.doi.org/10.1038/nmat1842>.
- [47] K.E. Sickafus, L. Minervini, R.W. Grimes, J.A. Valdez, M. Ishimaru, F. Li, K.J. McClellan, T. Hartmann, Radiation tolerance of complex oxides, *Science* (80-) 289 (2000) 748–751. <http://dx.doi.org/10.1126/science.289.5480.748>.
- [48] C.L. Tracy, J. Shamblyn, S. Park, F. Zhang, C. Trautmann, M. Lang, R.C. Ewing, Role of Composition, Bond Covalency, and Short-range Order in the Disordering of Stannate Pyrochlores by Swift Heavy Ion Irradiation, *Phys. Rev. B* 94 (2016) 064102. <http://dx.doi.org/10.1103/PhysRevB.94.064102>.
- [49] S. Park, M. Lang, C.L. Tracy, J. Zhang, F. Zhang, C. Trautmann, P. Kluth, M.D. Rodriguez, R.C. Ewing, Swift heavy ion irradiation-induced amorphization of La<sub>2</sub>Ti<sub>2</sub>O<sub>7</sub>, *Nucl. Instrum. Methods Phys. Res. Sect. B Beam Interact. Mater. Atoms* 326 (2014) 145–149. <http://dx.doi.org/10.1016/j.nimb.2013.10.088>.
- [50] S. Park, M. Lang, C.L. Tracy, J. Zhang, F. Zhang, C. Trautmann, M.D. Rodriguez, P. Kluth, R.C. Ewing, Response of Gd<sub>2</sub>Ti<sub>2</sub>O<sub>7</sub> and La<sub>2</sub>Ti<sub>2</sub>O<sub>7</sub> to swift-heavy ion irradiation and annealing, *Acta Mater.* 93 (2015) 1–11. <http://dx.doi.org/10.1016/j.actamat.2015.04.010>.
- [51] S. Park, M. Lang, C.L. Tracy, F. Zhang, C. Trautmann, Z. Wang, R.C. Ewing, Synchrotron x-ray diffraction analysis of gadolinium and lanthanum titanate oxides irradiated by xenon and tantalum swift heavy ions, *MRS Proc.* 1743 (2015). <http://dx.doi.org/10.1557/opl.2015.205>.
- [52] G.C. Lau, T.M. McQueen, Q. Huang, H.W. Zandbergen, R.J. Cava, Long- and short-range order in stuffed titanate pyrochlores, *J. Solid State Chem.* 181 (2008) 45–50.
- [53] C.L. Tracy, M. Lang, F. Zhang, C. Trautmann, R.C. Ewing, Phase transformations in Ln<sub>2</sub>O<sub>3</sub> materials irradiated with swift heavy ions, *Phys. Rev. B* 92 (2015) 174101. <http://dx.doi.org/10.1103/PhysRevB.92.174101>.
- [54] F.X. Zhang, J.W. Wang, M. Lang, J.M. Zhang, R.C. Ewing, Pressure-induced structural transformations in lanthanide titanates: La<sub>2</sub>TiO<sub>5</sub> and Nd<sub>2</sub>TiO<sub>5</sub>, *J. Solid State Chem.* 183 (2010) 2636–2643. <http://dx.doi.org/10.1016/j.jssc.2010.09.014>.
- [55] M.T. Paques-Ledent, Infrared and Raman studies of M<sub>2</sub>TiO<sub>5</sub> compounds (M = rare earths and Y): isotopic effect and group theoretical analysis, *Spectrochim. Acta Part A Mol. Spectrosc.* 32 (1976) 1339–1344. [http://dx.doi.org/10.1016/0584-8539\(76\)80177-8](http://dx.doi.org/10.1016/0584-8539(76)80177-8).
- [56] J. Shamblyn, M. Feygensohn, J. Neufeld, C.L. Tracy, F. Zhang, S. Finkeldei, D. Bosbach, H. Zhou, R.C. Ewing, M. Lang, Probing Disorder In Isometric Pyrochlore and Related Complex Oxides, *Nat. Mater.* 15 (2016) 507–512. <http://dx.doi.org/10.1038/NMAT4581>.
- [57] J. Wang, M. Lang, R.C. Ewing, U. Becker, Multi-scale simulation of structural heterogeneity of swift-heavy ion tracks in complex oxides, *J. Phys. Condens. Matter* 25 (2013) 135001. <http://dx.doi.org/10.1088/0953-8984/25/13/135001>.
- [58] G. Sattonnay, L. Thomé, I. Monnet, C. Grygiel, C. Legros, Effects of electronic energy loss on the behavior of Nd<sub>2</sub>Zr<sub>2</sub>O<sub>7</sub> pyrochlore irradiated with swift heavy ions, *Nucl. Instrum. Methods Phys. Res. Sect. B Beam Interact. Mater. Atoms* 286 (2012) 254–257. <http://dx.doi.org/10.1016/j.nimb.2011.11.017>.
- [59] W. Ostwald, Studien über die Bildung und Umwandlung fester Körper, *Z. Phys. Chem* 22 (1897) 289–302 [https://commons.wikimedia.org/wiki/File:Wider\\_das\\_Schulelend.pdf/npapers2://publication/uuid/A225B88D-E669-4E88-9945-396034E0F628](https://commons.wikimedia.org/wiki/File:Wider_das_Schulelend.pdf/npapers2://publication/uuid/A225B88D-E669-4E88-9945-396034E0F628).
- [60] W.J. Weber, J.W. Wald, H. Matzke, Effects of self-radiation Gd<sub>2</sub>Ti<sub>2</sub>O<sub>7</sub> and CaZrTi<sub>2</sub>O<sub>7</sub>, *J. Nucl. Mater.* 138 (1986) 196–209.
- [61] A. Chartier, G. Catillon, J. Crocombette, Key Role of the Cation Interstitial Structure in the Radiation Resistance of Pyrochlores, 155503, 2009, pp. 5–8.
- [62] R. Devanathan, F. Gao, C.J. Sundgren, Role of cation choice in the radiation tolerance of pyrochlores, *RSC Adv.* 3 (2013) 2901–2909.
- [63] R. Devanathan, W.J. Weber, J.D. Gale, Radiation tolerance of ceramics—insights from atomistic simulation of damage accumulation in pyrochlores, *Energy Environ. Sci.* 3 (2010) 1551.